Journal of Advanced Research xxx (xxxx) xxx

Contents lists available at ScienceDirect

Journal of Advanced Research

journal homepage: www.elsevier.com/locate/jare

Original Article

Structural and dynamic determinants for highly selective RET kinase inhibition reveal cryptic druggability

Moustafa A. Shehata [a,b], Julia Contreras [a], Ana Martín-Hurtado [a], Aurane Froux [a], Hossam Taha Mohamed [c,d], Ahmed A. El-Sherif [b], Iván Plaza-Menacho [a,*]

[a] Kinases, Protein Phosphorylation and Cancer Group, Structural Biology Programme, Spanish National Cancer Research Center (CNIO), Madrid 28029, Spain
[b] Chemistry Department, Faculty of Science, Cairo University, Giza 12613, Egypt
[c] Zoology Department, Faculty of Science, Cairo University, Giza 12613, Egypt
[d] Faculty of Biotechnology, October University for Modern Sciences and Arts, Giza 12451, Egypt

HIGHLIGHTS

- The druggability landscape of the RET active site is determined by the structural dynamics of the P-loop and the αC helix.
- RET selectivity is achieved by the occupancy of a small cryptic pocket adjacent to catalytic lysine defined by K758, L760, E768 and L772: the post-lysine pocket.
- Efficient occupancy of the post-lysine pocket is restricted to a synchronous P-loop open and αC-in configuration, a distinctive feature of RET crystal structures.
- LOXO-292 and BLU-667 target the post-lysine pocket and exploit extensive ATP mimicry.
- Engineered mutants targeting the post-lysine pocket impact on inhibitor binding and sensitivity, as well as RET tyrosine kinase activity.

GRAPHICAL ABSTRACT

First-generation RET inhibitors were multi-tyrosine kinase inhibitors (TKIs) derived from secondary pharmacology targeting the adenine-binding pocket that resulted in poor clinical outputs. Recently developed second-generation RET inhibitors (primary pharmacology derived) exploit in addition further vulnerabilities within the active site e.g. the post-lysine pocket (PKP). We define the structural and dynamical determinants conferring high selectivity to these inhibitors agaisnt RET by targeting the PKP, making them clinically successful.

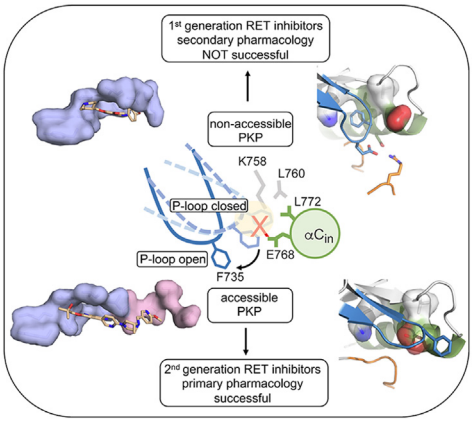

ARTICLE INFO

Article history:
Received 23 August 2021
Revised 5 April 2022
Accepted 5 May 2022
Available online xxxx

Keywords:
Protein kinases
Oncogene

ABSTRACT

Introduction: The structural and dynamic determinants for highly selective RET kinase inhibition are poorly understood.
Methods-objective: Here we demonstrate by applying an integrated structural, computational and biochemical approach that the druggability landscape of the RET active site is determined by the conformational setting of the ATP-binding (P-) loop and its coordination with the αC helix.
Results: Open and intermediate P-loop structures display additional druggable vulnerabilities within the active site that were not exploited by first generation RET inhibitors. We identify a cryptic pocket adjacent to the catalytic lysine formed by K758, L760, E768 and L772, that we name the post-lysine pocket,

Peer review under responsibility of Cairo University.
* Corresponding author.
E-mail address: iplaza@cnio.es (I. Plaza-Menacho).

https://doi.org/10.1016/j.jare.2022.05.004
2090-1232/

Structure-function
Targeted-therapies
Drug-discovery

with higher druggability potential than the adenine-binding site and with important implications in the regulation of phospho-tyrosine kinase activity. Crystal structure and simulation data show that the binding mode of highly-selective RET kinase inhibitors LOXO-292 and BLU-667 is controlled by a synchronous open P-loop and αC-in configuration that allows accessibility to the post-lysine pocket. Molecular dynamics simulation show that these inhibitors efficiently occupy the post-lysine pocket with high stability through the simulation time-scale (300 ns), with both inhibitors forming hydrophobic contacts in the pocket further stabilized by pi-cation interactions with the catalytic K758. Engineered mutants targeting the post-lysine pocket impact on inhibitor binding and sensitivity, as well as RET tyrosine kinase activity.

Conclusions: The identification of the post-lysine pocket as a cryptic druggable vulnerability in the RET kinase and its exploitation by second generation RET inhibitors has important implications for future drug design and the development of personalized therapies for patients with RET-driven cancers.

Introduction

Protein kinases play a causative role in human disease and cancer when deregulated by oncogenic mutations or overexpression [1]. A current hallmark for precision and personalized medicine is the development of highly specific protein kinase inhibitors that can be translated into the clinic for the successful treatment of cancer patients [2]. To date, the U.S. Food and Drug Administration (FDA) has approved more than 30 kinase inhibitors that are used in the clinic to treat cancer and other human disorders [3]. However, these drugs target only a small percentage of the entire human kinome (5%) and they usually display non-specific crosstalk and lack of activity against drug-resistant secondary mutations [3].

The *RET* (REarranged-during Transfection) proto-oncogene encodes a receptor tyrosine kinase for members of the glial cell line-derived neurotrophic factor (GDNF) family of extracellular ligands [4]. Oncogenic *RET* mutations and rearrangements results in constitutive ligand-independent activation of RET catalytic activity and signalling [4]. Both fusions and mutated RET are actionable drivers in non-small cell lung cancer (NSCLC) and thyroid cancers [5,6]. In particular, *RET* rearrangements have been identified in ∼ 2% of lung adenocarcinomas (NSCLC), 20% of papillary thyroid carcinoma (PTC), and less frequently in other types of cancer including breast, salivary gland intraductal carcinoma, pancreatic and colon cancers [5–9].

Rational and precise targeting of oncogenic drivers is a crucial hallmark in the cancer research field. Over the last years, the FDA approved the repurposing of several multi-tyrosine kinase inhibitors (MKIs) with pharmacological activity against RET for the treatment of thyroid, lung adenocarcinoma and other RET-positive cancers [10]. These inhibitors tested in the clinic had significant limitations due to non-selective activity against multiple kinases, dose-limiting toxicities as well as suboptimal target inhibition in the presence of resistance-associated secondary mutations, resulting altogether in modest survival outcomes in a limited subset of patients compared with other targeted therapies clinically successful. Overall, the clinical outcomes in response to RET-directed therapies were limited and modest compared with those achieved with other drugs targeting other oncogenes in solid tumors including EGFR, B-RAF, ALK, and ROS1 [11,12].

Recently developed RET inhibitors LOXO-292 (selpercatinib) and BLU-667 (pralsetinib) exhibited greater than 100-fold selectivity against a wide variety of RET oncogenic mutations in preclinical and clinical models [13–15]. Data from the phase I clinical trial (ARROW) revealed that BLU-667 treatment resulted in a substantial response in RET-rearranged NSCLC patients with overall response rate (ORR) of 60% and disease control rate (DCR) of 100% [14]. Additionally, clinical global phase I/II trial of LOXO-292 (LIBRETTO-001) for RET rearranged-positive NSCLC showed substantial response as a potent inhibitor with ORR of 68%, median progression-free survival (PFS) of 18.5 months, and median duration of response of 20.3 months [13,15]. LOXO-292 also demonstrated a high ORR of 91% in NSCLC patients with central nervous system metastasis [16,17]. In the registration dataset of RET-mutant MTC, the acquired clinical trial data showed ORR of 56% and 53%, in multi-kinase inhibitors (MKI)-treated and MKI-naive patients, respectively [15]. Another clinical study including 26 patients with RET-fusion positive PTC showed 62% ORR [18]. As a consequence, the FDA recently approved LOXO-292 and BLU-667 for the treatment of cancer patients presenting oncogenic *RET* rearrangements or mutations [16,19]**.** Despite such promising scenario, recurrent mechanisms of resistance to these selective inhibitors have already been described [20–22]. In particular, refractory mutations located at the solvent front pocket [21]. Understanding these mechanisms of resistance as well as the structural dynamics and pharmacophoric features required for highly specific and effective RET kinase inhibition is a crucial step for the design and development of clinically successful compounds able to overcome refractory RET mutations**.** In this study we apply an integrated approach combining structural, molecular dynamic simulations, together with functional analyses in order to define the druggability landscape of the RET active site and the molecular mechanism behind highly selective second generation RET inhibitors LOXO-292 and BLU-667.

Material and methods

Mapping of ligand binding site and hotspot residues

FTSite server [23] was used to explore the druggable pockets within the active site of RET in crystal structures with different P-loop conformations including closed- (PDB 2IVS), intermediate- (PDB 2IVT), and open- conformers (PDB 5AMN).

Transient pocket analyses

Mapping of transient pockets within the RET active site was performed by the TRansient Pockets in Protein (TRAPP) pipeline [24,25]. The overall workflow of the TRAPP webserver consists of three stages: i) ensemble of the generated structures, ii) superimposition and clustering and iii) detection and characterization. The TRAPP structure module contains several simulation methods for the generation of protein ensembles. The pseudo-ligand (RIPlig) and Langevin rotamerically induced perturbations (L-RIP) MD-based methods were used for the generation of protein ensembles. Following each perturbation, the structures were relaxed for 0.6 ps in an implicit solvent MD simulation coupled to a Langevin thermostat. The TRAPP analysis module was used to align and superimpose the generated structures using the backbone of the previously

chosen binding pocket residues using the RMSD metric, and clustered using a hierarchal algorithm with an RMSD threshold value of 3 Å. The TRAPP pocket module was employed to identify transient regions within the active site. The protein cavities near the binding pocket are calculated and saved on the grid. Furthermore, the physicochemical properties of the side chain residues in the detected cavities, surface area, and pocket are computed by this module.

Classical MD simulation

MD simulation was performed using the Amber 16 software package with GPU acceleration [26]. In particular, the ff14SB [27] and GAFF (generalized Amber force field) [28] for proteins and ligands, respectively, and the TIP3P model was chosen for water molecules. The partial charges of each ligand were calculated and implemented in the AM1-BCC charge method using the Antechamber module from AmberTools 16. Proteins were protonated at pH 7.4 and each molecular ensembled was immersed in a cubic box with a separation margin from the surface of the solute of 10 Å. The system was electroneutralized by addition of sufficient Cl^- counterions. The long-range electrostatic interactions were treated by the Particle Mesh Ewald (PME) method [29], while the short-range interactions; electrostatic and van der Waal, were calculated with a distance cut-off of 8 Å. The SHAKE algorithm [30] was applied to constrain the bond lengths involving hydrogen atoms to their equal volumes. The integration time step was 2 fs. The systems were energy minimized in two stages (a total of 5000 steps): I) Minimization of water molecules around the solute was run for 5000 steps, with 4000 steps of steepest descent and then 1000 steps of a conjugate gradient algorithm with a restraint force of 10 Kcal/mol$Å^2$ applied to restrain the solute atoms; II) Minimization of the entire system was run for the same number of steps as the previous stage, but with no restraint force applied. Following that, each system was heated to 300 °C in an NVT ensemble for 150 ps with a positional restraint of 10 Kcal/mol$Å^2$ applied to protein atoms. The system pressure was then held constant at 1 atm for 1 ns under NPT ensemble. Finally, the production phase was carried out for 300 ns under NPT ensemble at 300 K and 1 atm with no positional constraints. The system coordinates were saved every 10 ps. The generated trajectories were analyzed using CPPTRAJ from the AmberTools 17. Finally, hydrogen bond analysis was carried out by VMD hydrogen bonds tools with distance and angle cut-offs of 3.0 Å and 135°, respectively. All the plots were generated by Gnuplot and Python matplotlib [31].

Binding free energy calculations using MM-GBSA method

The Molecular Mechanics Generalized Boltzmann Surface Area (MM-GBSA) method was employed for binding free energy calculations using an implicit solvent model. This method additionally allows the energy decomposition analysis, which provides detailed information about the residual energetic contributions [32,33]. The free energy of ligand (L) binding to the receptor (R) to form a complex is estimated using the following equations:

$$\Delta G_{(bind)} = G_{(RL)} - G_{(R)} - G_{(L)}$$

It is further decomposed into several contributed interactions:

$$\Delta G_{(bind)} = \Delta H - T\Delta S = \Delta E_{(MM)} + \Delta G_{(sol)} - T\Delta S$$

In which:

$$\Delta E_{(MM)} = \Delta E_{(int)} + \Delta E_{(ele)} + \Delta E_{(vdw)}$$

$$\Delta G_{(sol)} = \Delta G_{(PB/GB)} + \Delta G_{(SA)}$$

$$\Delta G_{(SA)} = \gamma . SASA + b$$

ΔG bind is the interaction energy between the receptor and ligand in a vacuum, equivalent to the sum of polar (ΔG PB/GB) and non-polar (ΔG SA) interactions between the solute and the continuum solvent model. The GB model used for the calculation of polar interactions provides an analytical expression of the polar interactions, which is faster than the Poisson Boltzman (PB) method. The Generalized Boltzman (GB) model (ig = 2) was used to measure the electrostatic solvation energy [34]. The per residue energy decomposition method implemented in the MM/GBSA was used to analyze the residual energy interaction contribution to the total binding free energy. This method considers the intermolecular and solvation energies without the inclusion of the entropy [35].

Site directed mutagenesis

Site directed mutagenesis was performed on: i) a pBac-PAK-RET construct codifying codon optimized kinase domain (KD, aa 705–1013) and ii) pRC-CMV-RET isoform 9 (aa, 1–1072) as templates using a modified Q5-polymerase-based protocol in which complementary primers were employed followed by DpnI treatment at 37 °C for at least 120 min before transformation in Q5-DH5α bacterial strain. Mutagenesis was validated by Sanger sequencing.

Expression and purification of recombinant RET KD

Expression of (codon optimized) RET KD (WT and indicated mutants) was performed in Sf9 insect cells using a baculovirus system following already established and published protocols [36]. Protein purification was performed by tandem IMAC (Ni^{+2}) and Glutathione-beads gravity flow chromatography and in-gel 3C-protease digestion [36–38].

Differential scanning fluorimetry (DSF)

To evaluate the thermal stability of RET KD WT and indicated mutants in the absence of (apo) and in complex with inhibitors LOXO-292, BLU-667 and ZD6474 (vandetanib) as control, we applied two different DSF methods. First, an indirect SYPRO Orange-based method. For this assay the total reaction volume was adjusted to 40 μL at 1–2μM protein, 10 μM inhibitor, and 2X SYPRO Orange concentrations subjected to a gradient of temperature from 20 to 95 °C. Fluorescence was measured on an Applied Biosystem 7300 Real-Time PCR system. Second, a direct method based on changes in intrinsic fluorescence upon a quick gradient of temperature was measured using a tycho nanotemper instrument following manufactureŕs instructions.

Western-blotting

Western blotting (WBs) experiments were performed as previously described [38,39]. For auto-phosphorylation assays with recombinant proteins, 2.5–5 μM of isolated RET KD (WT and indicated mutants) was incubated with 2 mM $MgCl_2$ and 1 mM ATP for the indicated time points, after which samples were mixed with 5X sample loading buffer and boiled for 5 min. For cell lysates, transfected HEK293 cells subjected to the indicated concentrations of drug treatment were lysed in ice-cold 20 mM Tris pH 7.5, 150 mM NaCl, 2 mM DTT, 2.5% glycerol, supplemented with a cocktail of protease and phosphatase inhibitors (100X) and the total cell extract was centrifuged for 15 min at 5000–6000 rpm, after which soluble sample was mixed with 5X sample buffer and boiled for 5 min previous protein quantification with Bradford. Equal amounts of samples were run in SDS-PAGE gels and subjected to immunoblotting using the indicated antibodies.

Results

RET druggability is determined by the dynamics of the P-loop

We explored the druggability landscape of the RET active site (Fig. S1) under different P-loop configurations. Our rationale was driven by a previously solved high-resolution crystal structure of a RET KD displaying two discrete conformations of the P- loop [36]. In the closed structure the F735 (P-loop) side chain is clamped over the active site and the side chain of αC E768 points away from the cleft. This conformer was further stabilized by a triad of tethered residues between E734 (P-loop), R912 (activation loop, A-loop) and D771 (αC) (Fig. 1A). In contrast, in the open structure, the F735 side chain was solvent-exposed through a large displacement of the loop from the active site, whereas E768 points inward into the cleft. The two different conformations are defined by the mutually exclusive configurations of E768 and F735 side chains, which restrict nucleotide binding and accessibility. The open structure is further stabilized by salt-bridge and hydrogen bonding interactions between residues from the P- and the β3-αC loops (Fig. 1A). First, we measured the conformational space within the active site of RET using several crystal structures capturing different P-loop conformational states: 2IVS (closed), 2IVT (intermediate), 5AMN (open) and 4CKJ (open and closed), by calculating the center of mass distance between the β3 catalytic K758 side chain (NZ atom) and P-loop E734 main chain (Cα) and their corresponding active site volumes (Fig. 1B, and Table S1). While distances (and volumes) in the closed and intermediate states were 7.6 Å (646.6 Å^3) and 8.5 Å (902.2 Å^3), respectively, the open state showed significant larger values of 15.0 and 16.6 Å (1870.6 and 2311.7 Å^3). Transition from a closed to an open P-loop state was also associated with an increase in the distance between the gatekeeper residue V804 and the catalytic K758 (Table S1). These data indicated to us that a larger druggability space within the active site of RET is available in the opened structure. Next, we mapped druggable regions within the active site of RET susceptible to

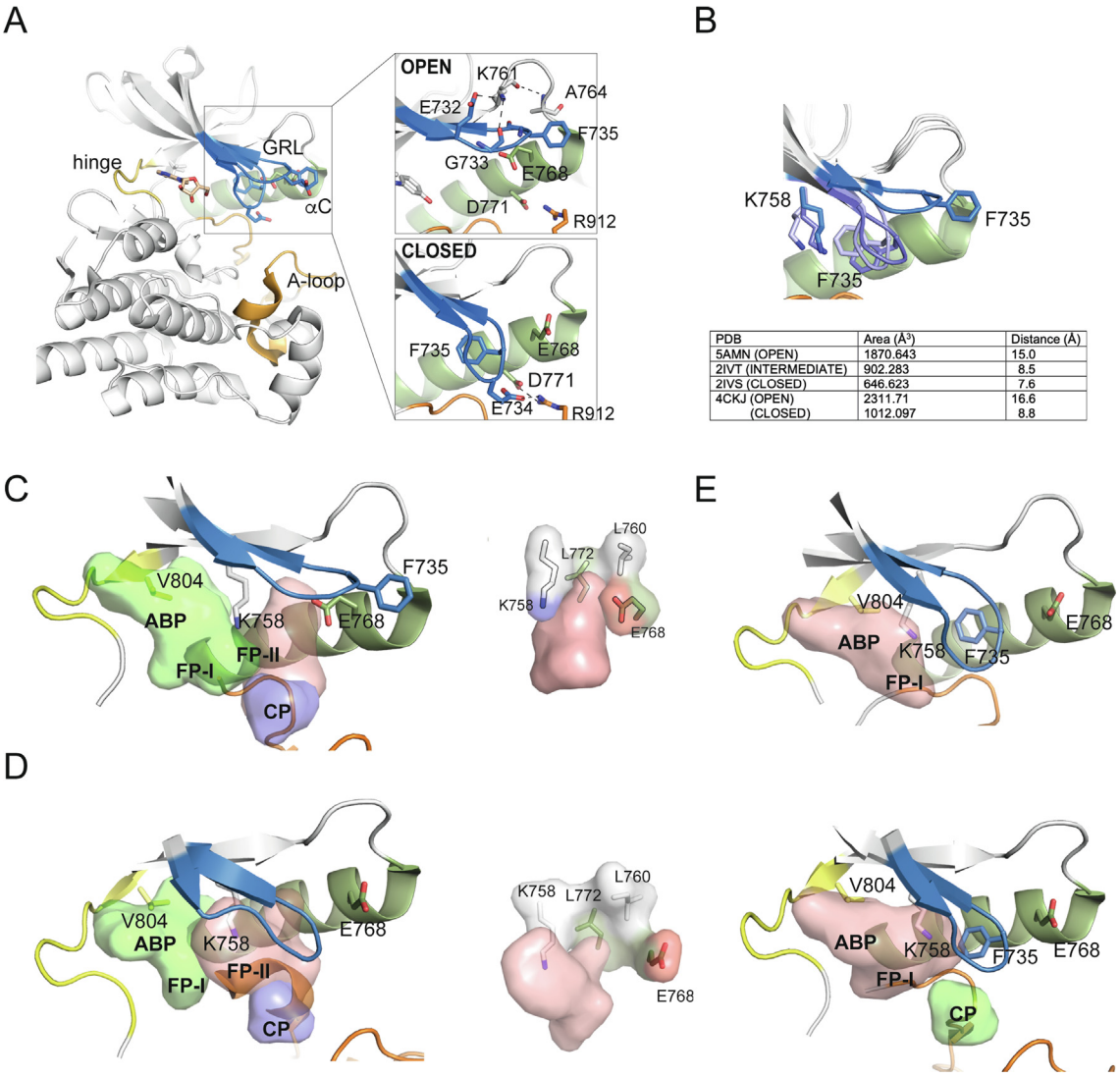

Fig. 1. RET active site druggability landscape is determined by the dynamics of the P-loop. (A) Cartoon representation of RET KD crystal structure with two discrete conformations of the P-loop (PDB 4CKJ). Hydrogen bonds and salt bridge interactions defining both open (upper) and close (lower) conformations. (B) Superimposition of the indicated RET KD crystal structures depicting side chains of F735 from the P-loop and catalytic K758 (β3) and their corresponding distances (Å) and defined volumes of the active site (Å^3) in each configuration. (C-E) FT-site mapping of druggable pockets within the active site (color coded) of RET under different P-loop configurations: (C) Open (PDB 5AMN), (D) intermediate (PDB 2IVT and 2IVV) and (E) closed (PDB 2IVS) depicting residues contributing to each pocket, ABP (adenine-binding pocket), FP-I and -II (front pocket-I and-II) and catalytic loop-HRD motif pocket (CP). Surface representation (C-D insets) with side-chain of residues defining a front subpocket-II defined by K758, L760, L772 and E775. Please note that a fully competent (available) pocket appears in the open crystal structure, being mutually exclusive with presence (occupancy) by the side chain of F775.

conformational changes by the P-loop using the FTSite (Fig. 1C-E and Table S2).

Three pockets were identified and ranked within the active site of RET in the open structure (Fig. 1C). The adenine-binding pocket (ABP) linked to the front pocket-I (FP-I), and gatekeeper pocket (in green) displayed average druggable scores. A small pocket adjacent to the catalytic loop-HRD motif pocket (CP, purple) made up of D874, R878, N879 and P914 side chains together with R912 main chain was detected with low druggability score (see Table S2 for details). Interestingly, a small pocket with maximum druggability potential was detected in the front-pocket-II (FP-II) adjacent to the catalytic lysine (in pink) defined by K758 (β3), L760 (β3-αC loop), E768 (αC), and L772 (αC). In the case of the intermediate structure (Fig. 1D, right panel) the ABP and FP-I (pink) ranked as the top druggable pocket. The CP (green) was also detected with averaged druggable potential. We noticed that the FP-II was not detected as it was partially occupied by the P-loop, in particular F735 side chain (Fig. 1D, right panel). This is in contrast with another intermediate RET crystal structure in which F735 side chain electron density is not defined (PDB 2IVV). In this situation the FP-II is partially accessible and appears as the top ranked druggable region (Fig. 1D, left and central panels). In the case of the closed structure (Fig. 1E) only the ABP and FP-I region appear as druggable. This is attributed to the degree of occupancy of the active site by F735 side chain and the P-loop itself impeding the access to the front solvent pocket-II. These data highlight: i) the existence of additional druggable vulnerabilities within the active site that were not exploited by first generation RET inhibitors, and ii) that optimal and selective RET kinase inhibition will depend on interactions other than those taking place at the adenine-binding and gatekeeper pockets.

Extensive perturbation of the active site disrupts the closed tether by inducing an open P-loop

To simulate the perturbation of the active site of RET by an inhibitor able to exploit an extensive druggable space and its impact on the transition from a closed to an open P-loop, we applied RIP (rotamerically induced perturbations) MD simulations methods. The RIP-MD method is a recent MD simulation technique that allows the generation of local perturbations in proteins that are capable of inducing large conformational changes of several Å in just picoseconds of a MD simulation [24]. It is particularly useful for identifying potentially mobile loops and helices in a protein structure, with important implications also in drug binding and catalytic inhibition. First, we used the RIPlig (RIP by a pseudo-ligand) method to identify large conformational changes within the active site. In the case of RET, this approach resulted in a significant 10 Å displacement of the P-loop from a closed tether to a fully open solvent accessible configuration as indicated by a large displacement of E734 (Fig. S2A). These data were in good agreement with the crystal structure data [36] and the rationale of our study (see Fig. 1A). Next, we applied the Langevin-RIP (L-RIP) approach by perturbing the dihedral angles of residues E734 and F735, both key determinants from our MD and X-ray data, to evaluate their specific contribution in P-loop transition (Fig. S2B). Perturbation of the dihedral angles of these two residues resulted in intermediate P-loop configurations associated with significant changes in the druggability potential and modification of active site physicochemical properties. Whereas perturbation of E734 (trajectory 1, Trj-1) resulted in lower and less consistent conformational changes in the P-loop and druggability, as indicated by volume and exposure values. Other physicochemical properties e.g. hydrophobicity, hydrogen acceptor, and negative ion dependencies were increased in some particular frames. On the other hand, F735 (Trj-2) perturbation resulted in higher druggability potential and the induction of complex conformational changes, as evidenced by higher volume and exposure values, which in turn resulted in increased hydrophobicity, hydrogen acceptor, and negative charges of the active site (Fig. S2B). Furthermore, we found that residues from the P-loop (aa 730–739), αC helix (aa 766–773), β3-αC loop (aa 756–760) and hinge (aa 805–810) regions showed highly dynamic behavior (Fig. S2C) indicative of significant motions by the P-loop and its coordination with other secondary structural elements such the αC helix, β3-αC loop and hinge. Furthermore, the two trajectories revealed several druggable pockets within the active site with high occurrence throughout the simulation (Fig. S2D) that matched the druggable space observed in the open and intermediate crystal structures by the FTSite method comprising the ABP, FP-I and FP-II (Fig. S2E). These results were in good agreement with the FTSite analyses and showed that perturbation of the closed autoinhibitory tether causes a large conformational motion of the P-loop expanding the druggability landscape of the RET kinase active site.

Identification and dynamic characterization of a cryptic and druggable pocket

The FTSite analyses revealed a sub-pocket adjacent to the catalytic lysine consisting of K758 (β3), L760 (β3-αC loop), E768 (αC), and L772 (αC) that we name post-lysine pocket (Fig. 1C). This pocket is defined in a central axis by hydrophobic L760 and L772, which are flanked on one side by catalytic K758 and E768 on the other (Fig. 1C-D). While in the closed and intermediate configurations F735 points to the center of the pocket, in the open structure F735 points away from the cleft and the side chain of E768 adopts and inner position together with K758, defining a fully accessible post-lysine pocket (Fig. 2A). We consistently observed an invariant αC helix-in (active) in the different configurations with a proper alignment of the regulatory and catalytic spine residues in a DFG-in state (Fig. S3). This newly identify druggable pocket appears to be evolutionary conserved (Fig. 2B). Next, we examined the presence and conservation of the FP-II and post-lysine pocket in other protein kinases that are pharmacologically inhibited by RET tyrosine kinase inhibitors [40] for which crystal structure data are available (Fig. 2C), including ALK (PDB 4TT7), VEGFR1 (3HNG), VEGFR2 (3VHE), MET (3DKC), Tie-2 (2OSC), TrKB (4ASZ), Axl (5U6B), ROS1 (3ZBF), FGFR1 (4V05), FGFR2 (1GJO), FGFR3 (6LVM), FGFR4 (4XCU), c-Src (4U5J), PDGFRα (6JOL), Abl (3IK3), EGFR (5Y9T) and B-RAF (3C4C). From this set of structures, we looked at the conservation of the residues defining the post-lysine pocket. RET F735 (P-loop) and L760 (β3-αC loop) were highly conserved residues within the dataset, with exceptions only in c-Abl (Y253) at the equivalent position to F735 and Tie-2 (M857) and Axl (M569) in the equivalent position to L760. An acidic residue equivalent to RET E768 (αC) lacked conservation in TrKB (A597), c-Src (S303), EGFR (A755) and B-RAF (Q494). RET L772 was substituted by phenylalanine in the case of ALK, Tie-2, TrKB, Axl, Ros, c-Src, Abl, B-RAF or isoleucine in the case of EGFR. These data indicate that the conservation of residues defining the post-lysine pocket occurred within the closest RET phylogenetic group of receptor tyrosine kinases (RTKs) including FGFR1, FGFR2, FGFR3, FGFR4, VEGFR1, VEGFR2, and PDGFRα (Fig. 2C and S4). Interestingly, the majority of the indicated structures have a closed P-loop and/or an αC-out configuration relative to RET, which results in a non-accessible post-lysine pocket (Fig. 2D-E). Using FTSite, a druggable post-lysine pocket was only detectable in structures with αC-in and open P-loop conformers including RET and FGFR2 (PDB 2PVF). In the latter, however, despite displaying an accessible post-lysine pocket the FP-II did not appear as druggable, probably as a consequence of the αC being slightly shifted toward an intermediate position (Fig. S4A). To further corroborate the dynamic

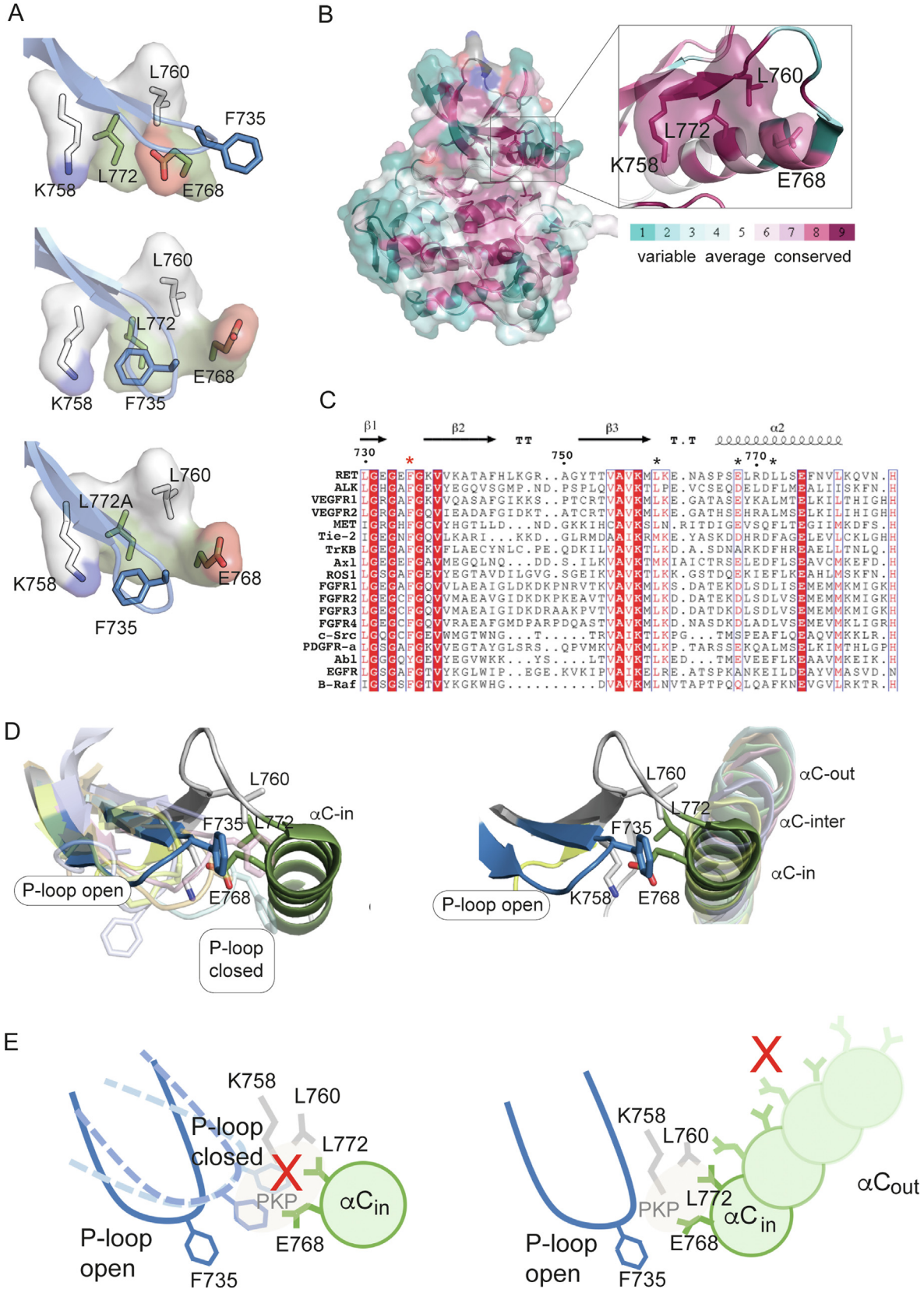

Fig. 2. Structural identification and dynamical characterization of a druggable post-lysine pocket. (A) Surface representation of RET post-lysine pocket composites under different P-loop configurations with amino acid side chains represented in sticks: open (PDB 5AMN), intermediate (PDB 2 IVT) and closed (PDB 2 IVS). In the case of RET a fully competent post-lysine pocket is available when the side chain of residue 735 is pointing away from the active site (open P-loop) and E768 is pointing inwards. (B) Evolutionary conservation of post-lysine pocket composites using Consurf [48], closer view of the pocket (inset, dark-red indicates high evolutionary rate). (C) Protein sequence alignment with secondary structural elements of a set of protein tyrosine kinases which are targets of known RET TKIs for which structural information is available showing conservation of post-lysine pocket residues (*). (D) Cartoon representation of a superimposition of crystal structures from (C) with RET post-lysine pocket residues depicted (RET, VEGFR1, VEGFR2, FGFR1, FGFR2, FGFR3, FGFR4 and PDGFRα). (E) Schematic representation of a competent post-lysine pocket: left panel, array of different P-loop configurations (from D versus RET αC-in). Right panel, array of different αC helices configurations (from D) versus RET open P-loop.

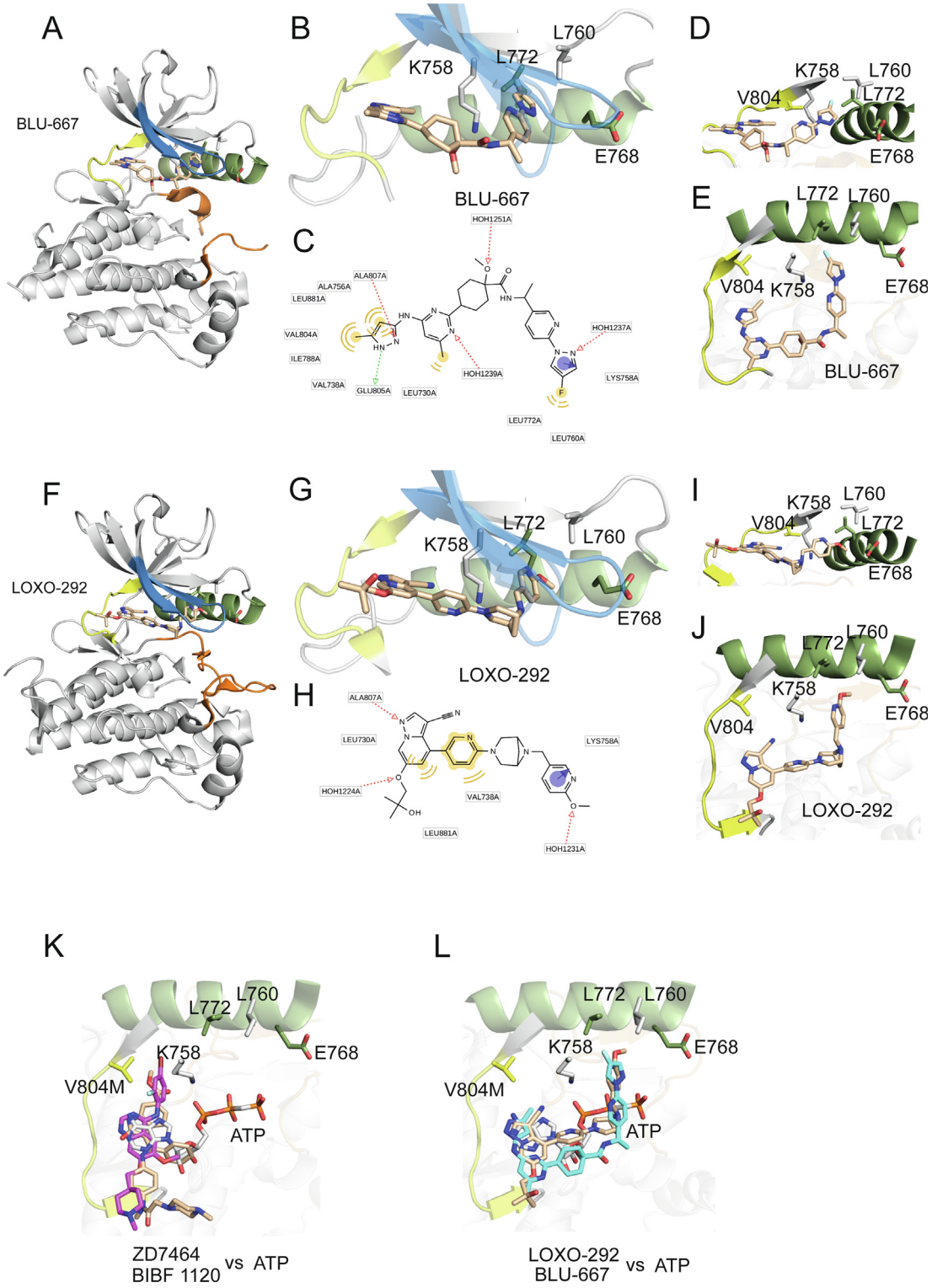

Fig. 3. LOXO-292 and BLU-667 target the post-lysine pocket. (A) Cartoon representation of RET KD crystal structure in complex with BLU-667 (PDB 7JU5) with colour coded secondary structural elements. (B) Close-up view of the active site in an open (PDB 7JU5) and superimposed closed P-loop (PDB 2IVS) configuration showing post-lysine pocket residues. (C) 2D-pharmacophore representation of BLU-667 interactions, in color coded: hydrophobic (yellow), hydrogen bond (red-donor, green-acceptor) and electrostatic interactions (pi-cation blue). (D) Lateral view of B, without depicting the P-loop. (E) Upper view from B, without depicting the P-loop. (F) Cartoon representation of RET kinase domain crystal structure in complex with LOXO-292 (PDB 7JU6) with colour coded secondary structural elements. (G) Close-up view of the active site in an open and closed P-loop configuration showing post-lysine pocket residues. (H) 2D-pharmacophore representation of LOXO-292 interactions, in color coded: hydrophobic (yellow), hydrogen bond (red-donor, green-acceptor) and electrostatic interactions (pi-cation blue). (I) Lateral view of G, without depicting the P-loop. (J) Upper view from G, without depicting the P-loop. Superimposition of the RET active site (upper view) with gate-keeper and post-lysine pocket residues, in complex with: (K) ATP (PDB 2PVF), ZD7464 (PDB 2IVU) AND BIBF1120 (6NEC), and (L) ATP based on a crystal structure of FGFR2 (PDB 2PVF), LOXO-292 (PDB 7JU6) and BLU-667 (PDB 7JU5).

crosstalk between the P-loop and αC helix to restrict or allow access to the post-lysine pocket, we analyzed the druggable pockets in the FGFR-3 active site using the FTSite. The catalytic domain of FGFR3 (PDB 6LVM) displayed a very similar conformation to FGFR2 with RMSD value of 0.6 Å, with αC-in but closed P-loop configuration. As predicted, neither the FP-II nor post-lysine pocket were identified as druggable sites in the FGFR3 structure (Fig. S4B).

These data demonstrated that conservation of the post-lysine pocket is a common feature of RET closest RTKs phylogenetic group, but this fact is not sufficient for occupancy as dynamic inputs from P-loop and αC restrict access to the pocket. A fully accessible and druggable post-lysine pocket requires of a P-loop-open and αC-in configuration that are only seen in RET kinase crystal structures, as illustrated in Fig. 2E.

LOXO-292 and BLU-667 target the post-lysine pocket

We explored the binding mode of highly specific RET inhibitors LOXO-292 and BLU-667 under different P-loop configurations. The two compounds were able to accommodate properly into the active site of RET only in an open state [21,22,41]. Superimposition with intermediate (2IVV) or closed (2IVS) RET structures (Fig. 3A-B and F-G) demonstrated that both compounds would clash with the loop in those settings in which compounds are restricted to accommodate only onto the adenine-binding pocket, as seen in the crystal structures of RET KD in complex with vandetanib and PP1 [36–38]. Opening of the P-loop results in suitable occupancy of the FP-II and the post-lysine pocket by LOXO-292 and BLU-667, respectively (Fig. 3A-B and F-G). Despite their atypical binding modes, both inhibitors do bind into a DFG-in (active) configuration with proper alignment of the regulatory (R-) and catalytic (C-) spines contrary to type II inhibitors, which perturb such alignment of the spines, see Fig. S3 [38,42,43].

BLU-667 (pralsetinib) targets the post-lysine pocket by accommodating the 4-fluoropyrazole ring into the patch forming a pi-cation interaction with the catalytic K758 and the fluorine group forming hydrophobic contacts with post-lysine pocket residues L760 and L772. Three hydrogen bonds were formed with E805 and A807 from the hinge region by the 5-methyl-pyrazol group with additional hydrophobic interactions with A756, V804, L881, I788 and V738. The methyl-pyrimidine group forms hydrophobic contacts with L730 in addition to coordinating with one water molecule via the N1. Of note there are two other water molecules coordinated with the compound: one with N2 of the 4-fluoropyrazole group, and the other with the methoxy oxygen bounded to the cyclohexane ring (Fig. 3B-E).

LOXO-292 (selpercatinib) targeted the post-lysine pocket by accommodating the 2-methoxypyridine ring and forming also a pi-cation interaction with K758. The pyrazolo[1,5-a] pyridine group forms an additional hydrogen bond with the main chain nitrogen atom of A807 at the hinge and hydrophobic interactions with L730 and L881. Further hydrophobic contacts were made by the central pyridine group and V738. Two water molecules are coordinated with the oxygen atoms from the 2-methoxypyridine group and the pyrazolo[1,5-a] pyridine ring, respectively (Fig. 3 G-J).

Both compounds appeared to exploit extensive ATP binding mimicry when compared to first-generation RET inhibitors whose prototypical interactions are mostly limited to the hinge and adenine-binding site. In fact, both compounds could only accommodate into the active site in an open state as the P-loop would clash with the compounds in the closed or intermediate configurations, in a manner reminiscent to what it does with ATP [36,44]. First generation type I RET inhibitors like vandetanib (ZD6474) and nindetanib (BIBF1120) get accommodated parallel to the hinge and perpendicular to the inner part of the αC helix (Fig. 3K). On the other hand, second-generation RET inhibitors accommodate in the path towards the P-loop below and in diagonal from the hinge across the proximal αC helix exploiting other druggable hotspots reaching to the solvent pocket, FP-I and FP-II (Fig. 3L). Taking as a reference the crystal structure of FGFR2 in complex with ATP (PDB 2PVF) [44], we observed the adenine group of ATP forming hydrogen bonds with E565 and A567 at the hinge mirroring the interactions of RET A807 and Y806 hinge residues with the pyrazolo-pyridine and methyl-pyrazol groups from LOXO-292 and BLU-667, respectively. Furthermore, hydrogen bonds between FGFR2 main chain N571 and R630 atoms and the ribose of the adenosine moiety were formed. In the case of RET equivalent residues e.g. L881 made hydrophobic contacts with the inhibitors and in the case of S811 it was shown to form a water bridge with the quinazoline group of vandetanib [37]. In FGFR2 the catalytic K515 (as part of the post-lysine pocket) form a salt bridge and hydrogen bonds with α and β phosphate groups, whereas in the case of RET the equivalent K758 formed pi-cation interactions with fluoropyrazole and methoxypyridine rings from BLU-667 and LOXO-292 respectively. FGFR2 F492 (equivalent to RET F735) and A491 (RETG733) main chain atoms formed hydrogen bonds with the γ-phosphate group of the ATP, and this was mirrored in the case of LOXO-292 crystal structure by two coordinated water molecules interacting with main chains G733 and E734 atoms from the P-loop. Altogether, these data demonstrate that LOXO-292 and BLU-667 target the post-lysine pocket by promoting the opening of the P-loop and exploiting extensive ATP mimicry, a feature not observed before with RET inhibitors of the first generation.

Molecular dynamics and stability of apo and complexed structures

The stability and dynamics of RET KD in the apo (PDB 2IVS) and in complex with LOXO-292 (PDB ID 7JU6), BLU-667 (PDB ID 7JU5) and ZD6474 (i.e. vandetanib, PDB ID 2IVU) were investigated using a 300-ns conventional MD simulation.

The root mean-square deviation (RMSD) of the protein Cα atom with respect to the initial frame was computed to assess the stability of each protein–ligand complex system compared with the apo state (Fig. 4A). Initial examination of the computed RMSD profile showed that all the complexed systems equilibrated rapidly with average fluctuations values of 2 Å. The apo system, on the contrary, displays significant conformational changes with average RMSD values above 2.5 Å, characterized by significant conformational changes in the P-loop (Fig. 4A).

We also used root-mean square fluctuation (RMSF) calculations to evaluate the effect of ligand binding on overall protein flexibility during the simulation process. General inspection of the RMSF profiles revealed a significant reduction in the P-loop flexibility by LOXO-292 and BLU-667 as a result of the occupation of the FP-II and post-lysine pocket, stabilizatioing the P-loop in an open conformation. RET-ZD6474 and apo, on the contrary, demonstrated high flexibility in the P-loop, which is consistent with the analysis of the average structure (Fig. 4B). These data together prove that LOXO-292 and BLU-667 have a direct impact on reducing the flexibility of the P-loop loop by forcing it to an open conformation that is required for post-lysine pocket occupancy.

Next, the MM/GBSA (molecular mechanics Boltzmann surface area) method [35,32] was used to estimate each inhibitor binding free energies (Table 1). The calculated binding free energy (G total) of RET-LOXO-292 and -BLU-667 complexed systems were −55.1 ± 4.1 and −49.1 ± 3.3 Kcal/mol respectively, which were significantly lower than the one observed for the RET-ZD6474 complex (-43.7 ± 2.6 Kcal/mol) indicative of higher binding affinities by the second-generation RET inhibitors. According to Table 1, the van der Waal interactions are the main drivers for the stability of LOXO-292 and BLU-667, with energies of −66.0 ± 3.2 and −61.7 ± 2.7 Kcal/mol, respectively (vs −52.9 ± 2.3

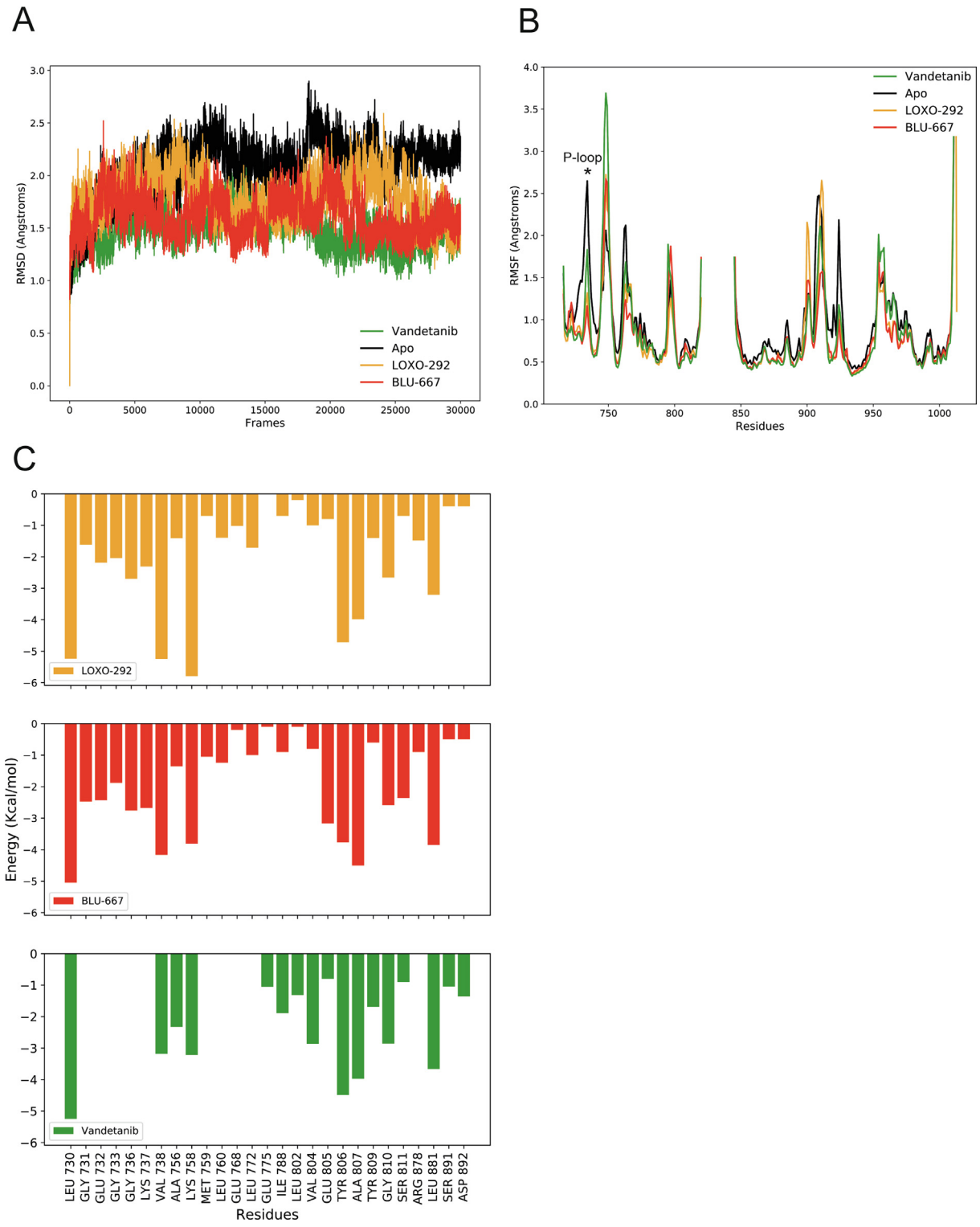

Fig. 4. Molecular dynamics and stability of apo and complexed structures. Computed (A) root mean-square deviation (RMSD), (B) root mean-square fluctuations (RMSF) of protein backbone Cα atoms and (C) per-residue energy decomposition for RET apo, LOXO-292, BLU-667 and ZD6474 complexes throughout the simulation.

Kcal/mol ZD6474). We also noticed that BLU-667 and ZD6474 have similar electrostatic interactions energies of −20.7 ± 4.4 and −21.0 ± 3.5 Kcal/mol, respectively with LOXO-292 having the lower electrostatic interaction energy of −10.7 ±4.5 Kcal/mol. These data were further corroborated by the per-residue energy decomposition analysis that identified the residues that contributed significantly to the ligand binding through intermolecular interactions (Fig. 4C). The distinct binding modes of LOXO-292 and BLU-667 that result in FP-II occupancy allowed the molecules to form strong interactions with P-loop residues G731, E732, G733, and G736, which stabilized the P-loop into an open-conformer. Despite access to the post-lysine pocket by LOXO-292 and BLU-667, the terminal 2-methoxypyridine moiety of LOXO-292 formed stronger interactions with the side chains

of K758, L760, E768, and L772. Furthermore, 2-methoxypyridine formed significant electrostatic interactions (cation-Pi) with the side chain of K758, resulting in an energy value of −5.8 Kcal/mol compared to BLU-667, which only formed a hydrophobic interaction and had an energy value of −3.8 Kcal/mol. LOXO-292 and BLU-667 appear to specifically interact with the R878 from the catalytic loop (Fig. 4C). Despite all the inhibitors formed hydrogen bonds with the hinge, gatekeeper pocket occupation by ZD6474 resulted in a stronger van der Waal interaction with the side chain of V804, making ZD6474 susceptible to acquired resistant mutations at that pocket. LOXO-292, BLU-667, and vandetanib all formed strong interactions with the solvent front region, in particular residue G810, with total energy values of −2.7, −2.6, and −2.9 Kcal/mol, respectively. Interestingly, refractory mutations at these sites that reduce the affinity of these inhibitors and confer resistance have been already identified in patients [41,45].

Functional evaluation of mutants targeting the post-lysine pocket reveals an impact on both inhibitor sensitivity and RET tyrosine kinase activity

In order to investigate the impact of post-lysine pocket residues on inhibitor binding and cellular response, we applied a multidisciplinary approach combining protein biochemistry, biophysics and cell-based assays. First, we generated recombinant RET KD WT and post-lysine pocket variants K758M, L760A, L772A and L760/772A (Fig. 5A). In addition, we also generated a KD V804M mutant as a negative control for the binding of a prototypical type-I inhibitor ZD6474. Next, we applied two independent DSF methods: i) a direct method measuring intrinsic fluorescence upon a fast temperature gradient providing an inflection temperature (T_i), and ii) an indirect method based on SYPRO^{TM} orange dye that provides melting temperatures (T_m). We measured the effect of LOXO-292 and BLU-667 binding on the thermal stability of the apo-control versus complexed proteins (Fig. 5B and Table 2), ZD-6474 was also tested as a negative control for the gatekeeper mutant V804M. While both LOXO-292 and BLU-667 binding to RET KD WT conferred a significant increment in the protein thermal (delta$T_{i/m}$) of about 10 °C. Mutations of some of the post-lysine pocket composites resulted in a significant effect on the binding of the inhibitors, in particular we observed a detrimental LOXO-292 binding effect to L772A with a lower Tm of 7.0 °C (vs 9.5 °C control WT), whereas the double mutant L760/772A had a larger BLU-667 Tm of 14.1 °C (vs 11.6 °C control WT). Furthermore, the K758M mutant displayed a significant thermal stability increment by LOXO-292 and BLU-667 of 11,9 and 14,2 °C (vs 9.5 and 11.6 °C control WT, respectively). The results from the K758M and double L760/772A mutants were surprising to some extend as we anticipated that perturbation of the post-lysine pocket composites would result in a detrimental effect on the binding on these inhibitors (see discussion). Next, we tested the effect of post-lysine pocket mutants on the phospho-tyrosine kinase activity of the RET KD in vitro in time course auto-phosphorylation assays (Fig. 5C). We found that, contrary to the L760A mutant, which displayed comparable levels to the WT, RET L772A had a loss of function effect on the tyrosine kinase activity as indicated by both total phospho-tyrosine and phospho-specific RET Y905 antibodies. The same detrimental effect was observed with the double L760/772A mutant. Finally, in order to recapitulate these results in cell-based assays we used HEK293 cells ectopically expressing a full-length RET receptor with a C634R mutation in the extracellular domain, which bypasses the GDNF ligand and co-receptor requirements for activation (with intact intracellular domain) subjected to a dose-dependent treatment with LOXO-292 and BLU-667 for 90 min (Fig. 5D). While treatment of RET WT KD with increasing concentrations of LOXO-292 and BLU-667 resulted in a consistent inhibition of RET auto-phosphorylation and ERK1/2 downstream activity at 10 nM, no significant differences were observed with the L760A mutant. In the case of the L772A mutant, as anticipated from the kinase assays we found a loss of function effect. Strikingly the double L760/772A mutant had a rescue effect on the tyrosine kinase activity by the L760A mutation, displaying also increased sensitivity to LOXO-293 and BLU-667 as 1 nM concentrations of the inhibitors resulted in a significant reduction on RET auto- and ERK1/2- phosphorylation levels. As a control we used RET KD V804M, which was sensitive to both LOXO-292 and BLU-667 at similar concentrations than the WT, but was resistant to ZD6474 treatment. These data were consistent with the DSF results, and showed the important implications of the post-lysine pocket composites on both inhibitor sensitivity and RET tyrosine kinase activity.

Discussion

LOXO-292 and BLU-667 are recently developed second-generation RET inhibitors with a potent and selective activity against a wide range of RET fusions and mutations in both preclinical and clinical models [13–15] with a remarkable patient response observed in phase I and II clinical trials [13–15,17]. The main purpose of this study is to explain the structural and dynamical determinants conferring high selectivity by these RET inhibitors through a comprehensive computational, structural and functional characterization. We defined the post-lysine pocket as a key structural determinant for efficient and selective RET kinase inhibition with important consequences on RET tyrosine kinase activity.

Extensive analysis of the active site showed that potent and selective RET kinase inhibition requires the exploitation of vulnerabilities beyond the occupation of the adenine- binding pocket and gate-keeper vicinity. We show that the intrinsic flexibility of the P-loop and the αC helix reshapes the druggability landscape in the RET active site (Fig. 1). While in the closed P-loop structure only the adenine-binding, gate-keeper and solvent pockets were potentially druggable, in the intermediate and open P-loop structures the FP-II appeared with a significant higher druggability potential relative to the adenine-binding site. This pocket is distinguished by the existence of a small cryptic sub-pocket adjacent to the catalytic lysine defined by K758, L760, E768, and L772 that we defined as the post-lysine pocket. This cryptic pocket was fully accessible in the case of the open RET structures. The assembly of these residues and the accessibility to the post-lysine pocket was regulated

Table 1
Values for the stability and binding free energies of the indicated inhibitors using Molecular mechanics Boltzmann surface area (MM/GBSA) method. The computed binding free energy (Kcal/mol) of RET in complex with LOXO-292, BLU-667 and ZD6474 are depicted.

Inhibitor	ΔEvdw	ΔEele	ΔGGB	ΔEsurf	ΔEgas	ΔGsolv	ΔGtotal
LOXO-292	−66.0 ± 3.2	−10.7 ± 4.5	28.9 ± 4.1	−7.4 ± 0.3	−76.6 ± 6.2	21.5 ± 4.0	−55.1 ± 4.1
BLU-667	−61.7 ± 2.7	−20.7 ± 4.4	40 ± 3.4	−6.9 ± 0.3	−82.4 ± 5.2	33.3 ± 3.3	−49.1 ± 3.3
ZD6474	−52.9 ± 2.3	−21.0 ± 3.5	36.5 ± 3.3	−6.2 ± 0.2	−73.9 ± 4.4	30.2 ± 3.2	−43.7 ± 2.6

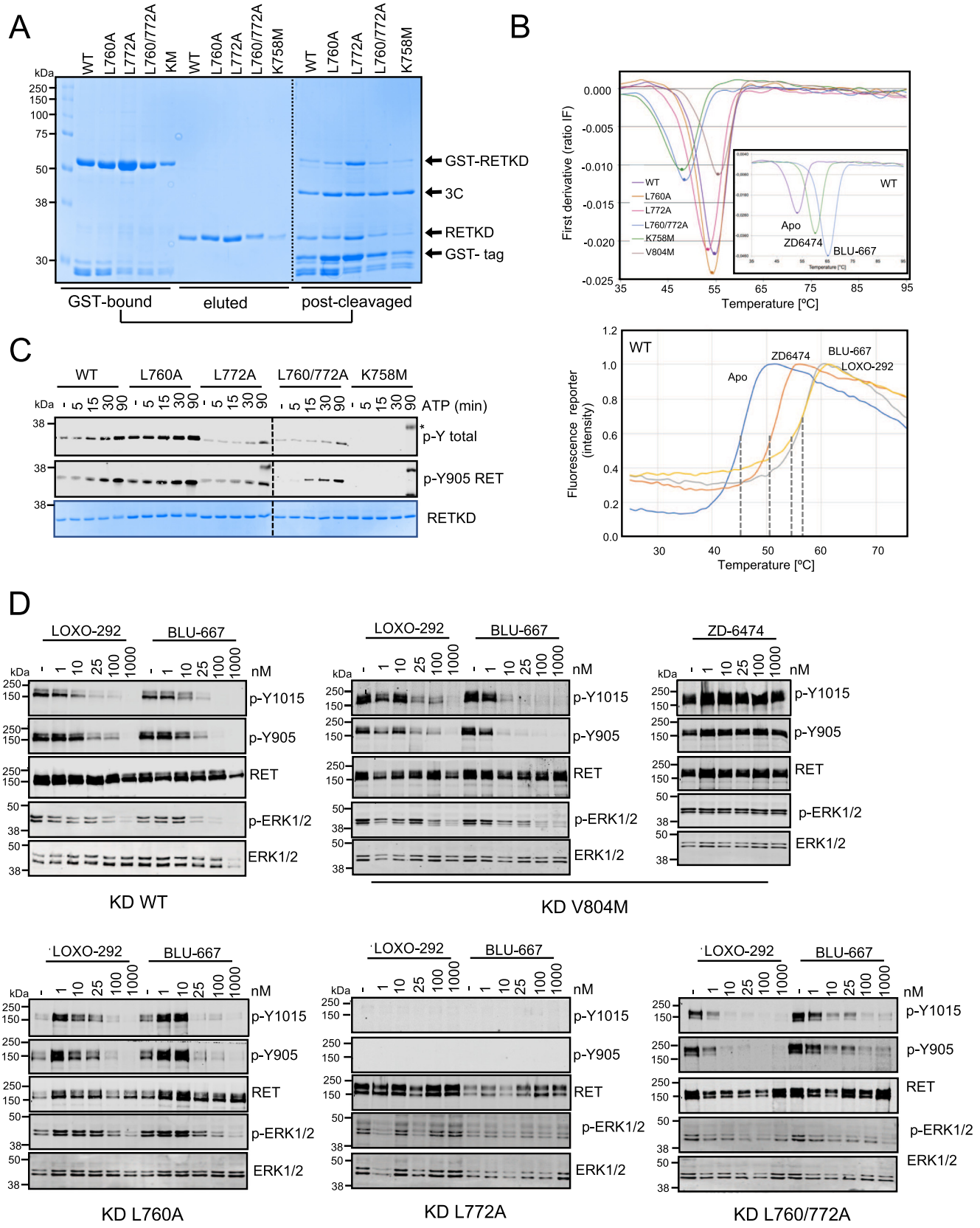

Fig. 5. Functional evaluation of mutants targeting the post-lysine pocket. (A) Coomassie staining of recombinant RET KD (WT and indicated mutants) samples from the different protein purification steps. (B) DSF analyses of apo and complexed proteins by direct IF (tycho nanotemper, upper panel) and SYPRO orange (lower panel) providing thermal shifts changes, T_i and T_m respectively. For illustrative purposes, a representative example of RET KD WT is depicted. See Table 2 for full dataset, please note that LOXO-292 samples were not measurable by IF (data not determined, nd). (C) WBs of auto-phosphorylation time courses (0–90 min) with recombinant RET KD WT and indicated mutants using total phospho-tyrosine and RET phospho-Y905 specific antibodies. Total protein levels were determined by Coomassie staining. (*, protein marker) (D) WBs data of lysates from HEK293 cells ectopically expressing RET WT or the indicated mutants treated with increasing concentrations of the inhibitors LOXO-292 and BLU-667 using the indicated antibodies. ZD6474 was used as an internal control for the RET KD V804M mutant.

Table 2
Differential Scanning Fluorometry (DSF) data measured by i) SYPRO™ Orange providing melting temperatures (Tm) and ii) intrinsic fluorescence (IF) providing inflection temperature (Ti,). Data shown mean ± standard deviation (SD) are from 4 to 8 independent experiments.

		Tm (°C)	deltaTm	Ti (°C)	deltaTi
WT	Apo	44.7 ± 0.7		55.9 ± 0.6	
	LOXO292	54.3 ± 1.7	9.5	n/d	
	BLU667	56.4 ± 0.5	11.6	66.9 ± 2.3	10.8
	ZD6447	51.1 ± 0.6	6.3	60.1 ± 1.5	4.7
L760A	Apo	42.9 ± 3.3		54.8 ± 1.1	
	LOXO292	51.6 ± 3.3	8.7	n/d	
	BLU667	54.8 ± 0.4	11.9	66.0 ± 1.0	11.2
	ZD6447	51.2 ± 0.6	8.3	60.1 ± 1.5	5.3
L772A	Apo	41.3 ± 1.5		53.0 ± 0.4	
	LOXO292	48.4 ± 3.8	7.1	n/d	
	BLU667	52.9 ± 1.1	11.7	65.0 ± 1.2	12.0
	ZD6447	49.1 ± 1.2	7.9	58.6 ± 2.2	5.6
L760/772A	Apo	36.4 ± 0.5		48.8 ± 0.3	
	LOXO292	46.8 ± 1.7	10.9	n/d	
	BLU667	50.5 ± 0.9	14.1	62.9 ± 0.7	14.0
	ZD6447	45.8 ± 0.6	9.3	56.9 ± 0.7	8.05
K758M	Apo	36.2 ± 0.2		49.9 ± 0.7	
	LOXO292	48.2 ± 2.9	11.9	n/d	
	BLU667	50.5 ± 0.1	14.2	61.8 ± 0.6	11.9
	ZD6447	45.2 ± 0,5	8.9	54.8 ± 1.3	4.8
V804M	Apo	47.2 ± 1.3		55.9 ± 0.4	
	LOXO292	53.6 ± 1.6	6.4	n/d	
	BLU667	55.8 ± 1.2	8.7	67.1 ± 1.6	11.1
	ZD6447	47.0 ± 1.7	−0.1	55.4 ±. 1.4	−0.5

by the position of F735 side chain, which is directly coordinated by the dynamics of the P-loop and the positioning of the αC helix. An interesting observation is that, as part of the adenine-binding site, the gatekeeper sub-pocket was found only in the structures with an intermediate and open P-loop configuration. This is related to the F735 side chain transitioning away from the post-lysine pocket, which creates more space for the K758 side chain. The recently discovered S904F mutation in the activation loop of RET resulted in acquired ZD6474 resistance [46]. The crystal structure of the RET KD S904F mutant (PDB 6FEK) revealed a closed P-loop conformer with an unusual K758 side chain rotamer with NZ atom pointing towards the gatekeeper pocket. A superimposition of this structure with the RET KD complexed to ZD6474 (PDB 2IVU) revealed steric clashes between the inhibitor and K758 side chain. This is further supported by a shorter V804-K758 distance when compared to other closed P-loop structures (table S1). In addition, long-unbiased MD simulation of RET KD WT and mutant S904F complexed with ZD6474 revealed higher energy state of the mutant kinase with intermediate P-loop configuration with F735 pointing towards the active site. As a result, we anticipate that K758 regulates the accessibility to the gatekeeper pocket via the crosstalk between the gatekeeper and the post-lysine pockets by the positioning of F735 side chain.

RIP MD simulations show that extensive (RIPlig) and site-directed (L-RIP) perturbation of the P-loop disrupts the close tether and induces an opening of the P-loop and active site, consequently expanding the druggability landscape, being F735 the key determinant for such transition (Fig. 2). Furthermore, we examined the presence and conservation of the FP-II and post-lysine pocket in other protein kinases that are pharmacologically inhibited by RET tyrosine kinase inhibitors for which structural information was available (Fig. 2 and S2). We found that conservation of the post-lysine pocket is also a common feature of the phylogenetically closer group of RTKs (i.e. FGFR1-4, VEGFR1-2), but is not sufficient for occupancy and competency as dynamic inputs from the P-loop and αC restrict access to the pocket. A fully accessible and druggable post-lysine pocket requires of a synchronous P-loop-open and αC-in configuration only seen in RET crystal structures.

Superimposition of RET KD crystals structures in complex with LOXO-292 and BLU-667 [21,22,41] with crystal structures of RET in complex with type-I inhibitors [37,38] showed that both compounds could only fit into the active site in an open P-loop state (Fig. 3), as in the closed or intermediate configurations it would clash with the compounds, in a reminiscent manner to ATP [36]. The free energy calculations by the MM/GBSA method shows that LOXO-292 and BLU-667 forms important interactions with L730 (β1) and V738 (β2), both from the P-loop, and also with hinge residues Y806, K808 and G810. Interestingly, refractory mutations in those sites have been found in patients and resistant cell lines and clones [21,41] . This is due to steric clashes with the inhibitors caused by the replacement of bulky amino acid chains in those regions, as well as the disruption of strong intermolecular hydrophobic contacts as shown by MM/GBSA analysis [45,47].

Functional characterization of mutants targeting the post-lysine pocket revealed a dual role on drug sensitivity and tyrosine kinase activity. The results from the double mutant (L760/772) and K758M were surprising as we anticipated that perturbation of the post-lysine pocket composites would result a priory in a detrimental effect on the binding on these inhibitors. However, a tighter binding was observed in these cases as indicated by increased T_m and T_i (Fig. 5 and Table 2). This can be potentially explained by the fact that substitutions by shorter side chains may allow a better accommodation of the compounds into the post-lysine pocket, resulting in a sensitizing effect as seen with the double mutant (L760/772A) (Fig. 5D). In auto-phosphorylation assays using recombinant isolated RET kinase, the L760A mutant appeared to have higher background phosphorylation levels which were slightly enhanced over the time course compared with WT (Fig. 5C). These results suggest the a L760A mutant could be a better substrate for Sf9 endogenous kinases, as seen before by both oncogenic mutations targeting the kinase domain (in particular M918T) and mutants disrupting the closed auto-inhibited tether [36]. On the contrary, L772A and L760/772A both had a significant detrimental effect on RET phospho-tyrosine kinase activity (Fig. 5C). When the same mutants were evaluated in a RET full-length context in dose-dependent cell-based assays (Fig. 5D) we obtained results in line with the recombinant protein data e.g. a loss of function effect by the L772A mutation. Strikingly we also found a rescue effect by the L760A mutation and increased sensitivity by the double mutant L760/772A. These data were supported

by the binding and DSF data where both L760/772A and the K758M mutants displayed a significant increment in their Tm and Ti upon inhibitor binding (Table 2). These results suggested that mutating specific post-lysine pocket components to alanine favored the binding potentially by allowing a better accommodation of the 2-methoxypyridine (LOXO-292) and 4-fluoropyrazole (BLU-667). Furthermore, the striking effect of the double mutant in terms of rescuing the null effect of the L772A mutation indicates a potential crosstalk between the β3-αC loop and the αC helix, together with L772, which forms part of a recently described PIF-like pocket in RET [38]. In both cases, there are clear signs of allosteric inputs to the catalytic site by regulating also R- and C-spines assemblies. We hypothesize that development of next generation RET inhibitors with improved selectivity and efficacy will require of chemical optimizations that will: i) minimize contacts and interactions with the solvent pocket and β3, ii) favor accommodation of the 2-methoxypyridine (LOXO-292) and 4-fluoropyrazole (BLU-667) groups into the post-lysine pocket, iii) provide larger space between the gate-keeper residue and the catalytic lysine to overcome gate-keeper drug resistant mutations and iv) target the catalytic loop pocket residues, according to our FTsite and MM/GBSA data. Altogether the identification of the post-lysine pocket as a cryptic druggable vulnerability in the RET kinase exploited by second generation RET inhibitors has important implications for future drug design and the development of more potent and specific (allosteric) inhibitors and personalized therapies for patients with RET-driven cancers.

Compliance with ethics requirements

This article does not contain any studies performed with human or animal subjects.

Author contributions

Conception of the study and experimental design (IP-M), manuscript writing and figure preparation (IP-M and MAS), experimental and bio-computational work (MAS, JC, AM-H, AF and IP-M), data processing and analysis (MAS and IP-M), academic mentoring to MAS (HTM, AAE).

Declaration of Competing Interest

The authors declare that they have no known competing financial interests or personal relationships that could have appeared to influence the work reported in this paper.

Acknowledgements

We would like to thank: the CNIO for supporting this study , the Genomics and Proteomics Units for their technical assistance and the Experimental Therapeutic Programme (ETP) and the Spectroscopy and Nuclear Magnetic Resonance Unit for sharing their expertise and providing helpful comments and scientific advice. We give special thanks to the family of Carmen Gloria Bonnet for their CNIO Friends contribution and suppport. This work was dedicated to Robert M. W. Hofstra (1962-2021), former PhD supervisor and mentor (IP-M).

Funding

We thank the Centro Nacional de Investigaciones Oncológicas (CNIO), which is supported by the Instituto de Salud Carlos III and recognized as a "Severo Ochoa" Centre of Excellence (ref. CEX2019-000891-S, awarded by MCIN/AEI/ 10.13039/501100011033) for core funding and supporting this study. This work was further supported by projects: BFU2017-86710-R funded by MCIN/ AEI /10.13039/501100011033 and ERDF "A way of making Europe", PID2020-117580RB-I00 funded by MCIN/ AEI /10.13039/501100011033, RYC-2016-1938 funded by MCIN/AEI /10.13039/501100011033 and ESF "Investing in your future", and a Marie Curie WHRI-ACADEMY International grant (number 608765) to IP-M and a CNIO-Friends predoctoral Carmen Gloria Bonnet Fellowship to MAS.

Appendix A. Supplementary material

Supplementary data to this article can be found online at https://doi.org/10.1016/j.jare.2022.05.004.

References

[1] Blume-Jensen P, Hunter T. Oncogenic kinase signalling. Nature 2001;411(6835):355–65.
[2] Zhang J, Yang PL, Gray NS. Targeting cancer with small molecule kinase inhibitors. Nat Rev Cancer 2009;9(1):28–39.
[3] Feng H. Tyrosine kinases as druggable targets in cancer 2019.
[4] Plaza-Menacho I. Structure and function of RET in multiple endocrine neoplasia type 2. Endocr Relat Cancer 2018;25:T79–90.
[5] Kohno T, Ichikawa H, Totoki Y, Yasuda K, Hiramoto M, Nammo T, et al. KIF5B-RET fusions in lung adenocarcinoma. Nat Med 2012;18(3):375–7.
[6] Lipson D, Capelletti M, Yelensky R, Otto G, Parker A, Jarosz M, et al. Identification of new ALK and RET gene fusions from colorectal and lung cancer biopsies. Nat Med 2012;18(3):382–4.
[7] Paratala BS, Chung JH, Williams CB, Yilmazel B, Petrosky W, Williams K, et al. RET rearrangements are actionable alterations in breast cancer. Nat Commun 2018;9(1). doi: https://doi.org/10.1038/s41467-018-07341-4.
[8] Skálová A, Vanecek T, Uro-Coste E, Bishop JA, Weinreb I, Thompson LDR, et al. Molecular Profiling of Salivary Gland Intraductal Carcinoma Revealed a Subset of Tumors Harboring NCOA4-RET and Novel TRIM27-RET Fusions: A Report of 17 cases. Am J Surg Pathol 2018;42(11):1445–55.
[9] Skálová A, Ptáková N, Santana T, Agaimy A, Ihrler S, Uro-Coste E, et al. NCOA4-RET and TRIM27-RET Are Characteristic Gene Fusions in Salivary Intraductal Carcinoma, Including Invasive and Metastatic Tumors: Is "Intraductal" Correct? Am J Surg Pathol 2019;43(10):1303–13.
[10] Redaelli S, Plaza-Menacho I, Mologni L. Novel targeted therapeutics for MEN2. Endocr Relat Cancer 2018;25(2):T53–68.
[11] Drilon A, Hu ZI, Lai GGY, Tan DSW. Targeting RET-driven cancers: lessons from evolving preclinical and clinical landscapes. Nat Rev Clin Oncol 2018;15:150.
[12] Schram AM, Chang MT, Jonsson P, Drilon A. Fusions in solid tumours: diagnostic strategies, targeted therapy, and acquired resistance. Nat Rev Clin Oncol 2017;14(12):735–48.
[13] Drilon A, Oxnard GR, Tan DSW, Loong HHF, Johnson M, Gainor J, et al. Efficacy of Selpercatinib in RET Fusion-Positive Non-Small-Cell Lung Cancer. N Engl J Med 2020;383(9):813–24.
[14] Subbiah V, Gainor JF, Rahal R, Brubaker JD, Kim JL, Maynard M, et al. Precision Targeted Therapy with BLU-667 for RET-Driven Cancers. Cancer Discov 2018;8(7):836–49.
[15] Wirth LJ, Sherman E, Robinson B, Solomon B, Kang H, Lorch J, et al. Efficacy of Selpercatinib in RET-Altered Thyroid Cancers. N Engl J Med 2020;383(9):825–35.
[16] Wright KM. FDA Approves Pralsetinib for Treatment of Adults With Metastatic RET Fusion-Positive NSCLC. Oncology (Williston Park) 2020;34(406–406):431.
[17] Guo R, Schreyer M, Chang JC, Rothenberg SM, Henry D, Cotzia P, et al. Response to Selective RET Inhibition With LOXO-292 in a Patient With RET Fusion-Positive Lung Cancer With Leptomeningeal Metastases. JCO Precis Oncol 2019(3):1–6. doi: https://doi.org/10.1200/PO.19.00021.
[18] Ackermann CJ, Stock G, Tay R, Dawod M, Gomes F, Califano R. Targeted Therapy For RET-Rearranged Non-Small Cell Lung Cancer: Clinical Development And Future Directions. Onco Targets Ther 2019;12:7857–64.
[19] Bradford D, Larkins E, Mushti SL, Rodriguez L, Skinner AM, Helms WS, et al. FDA Approval Summary: Selpercatinib for the Treatment of Lung and Thyroid cancers with RET Gene Mutations or Fusions. Clin Cancer Res 2021;27(8):2130–5.
[20] Lin JJ, Liu SV, McCoach CE, Zhu VW, Tan AC, Yoda S, et al. Mechanisms of Resistance to Selective RET Tyrosine Kinase Inhibitors in RET Fusion-Positive Non-Small Cell Lung Cancer. Ann Oncol 2020;31(12):1725–33.
[21] Solomon BJ, Tan L, Lin JJ, Wong SQ, Hollizeck S, Ebata K, et al. RET Solvent Front Mutations Mediate Acquired Resistance to Selective RET Inhibition in RET-Driven Malignancies. J Thorac Oncol 2020;15:541–9.
[22] Terzyan SS, Shen T, Liu X, Huang Q, Teng P, Zhou Mi, et al. Structural basis of resistance of mutant RET protein-tyrosine kinase to its inhibitors nintedanib and vandetanib. J Biol Chem 2019;294(27):10428–37.
[23] Kozakov D, Grove LE, Hall DR, Bohnuud T, Mottarella SE, Luo L, et al. The FTMap family of web servers for determining and characterizing ligand-binding hot spots of proteins. Nat Protoc 2015;10(5):733–55.

[24] Kokh DB, Czodrowski P, Rippmann F, Wade RC. Perturbation Approaches for Exploring Protein Binding Site Flexibility to Predict Transient Binding Pockets. J Chem Theory Comput 2016;12(8):4100–13.
[25] Stank A, Kokh DB, Horn M, Sizikova E, Neil R, Panecka J, et al. TRAPP webserver: predicting protein binding site flexibility and detecting transient binding pockets. Nucleic Acids Res 2017;45(W1):W325–30.
[26] Salomon-Ferrer R, Götz AW, Poole D, Le Grand S, Walker RC. Routine Microsecond Molecular Dynamics Simulations with AMBER on GPUs. 2. Explicit Solvent Particle Mesh Ewald. J Chem Theory Comput 2013;9 (9):3878–88.
[27] Maier JA, Martinez C, Kasavajhala K, Wickstrom L, Hauser KE, Simmerling C. ff14SB: Improving the Accuracy of Protein Side Chain and Backbone Parameters from ff99SB. J Chem Theory Comput 2015;11(8):3696–713.
[28] Wang J, Wolf RM, Caldwell JW, Kollman PA, Case DA. Development and testing of a general amber force field. J Comput Chem 2004;25(9):1157–74.
[29] Darden T, York D, Pedersen L. Particle mesh Ewald: An Nlog(N) method for Ewald sums in large systems. J Chem Phys 1993;98(12):10089–92.
[30] Ryckaert J-P, Ciccotti G, Berendsen HJC. Numerical integration of the cartesian equations of motion of a system with constraints: molecular dynamics of n-alkanes. J Comput Phys 1977;23(3):327–41.
[31] Hunter J, Henderson M, Khan I. Collaborative annotation of 3D crystallographic models. J Chem Inf Model 2007;47(6):2475–84.
[32] Wang E, Sun H, Wang J, Wang Z, Liu H, Zhang JZH, et al. End-Point Binding Free Energy Calculation with MM/PBSA and MM/GBSA: Strategies and Applications in Drug Design. Chem Rev 2019;119(16):9478–508.
[33] Zoete V, Irving MB, Michielin O. MM-GBSA binding free energy decomposition and T cell receptor engineering. J Mol Recognit 2010;23(2):142–52.
[34] Onufriev A, Bashford D, Case DA. Exploring protein native states and large-scale conformational changes with a modified generalized born model. Proteins 2004;55(2):383–94.
[35] Genheden S, Ryde U. The MM/PBSA and MM/GBSA methods to estimate ligand-binding affinities. Expert Opin Drug Discov 2015;10(5):449–61.
[36] Plaza-Menacho I, Barnouin K, Goodman K, Martínez-Torres Rubén J, Borg A, Murray-Rust J, et al. Oncogenic RET kinase domain mutations perturb the autophosphorylation trajectory by enhancing substrate presentation in trans. Mol Cell 2014;53(5):738–51.
[37] Knowles PP, Murray-Rust J, Kjær S, Scott RP, Hanrahan S, Santoro M, et al. Structure and chemical inhibition of the RET tyrosine kinase domain. J Biol Chem 2006;281(44):33577–87.
[38] Plaza-Menacho I, Barnouin K, Barry R, Borg A, Orme M, Chauhan R, et al. RET Functions as a Dual-Specificity Kinase that Requires Allosteric Inputs from Juxtamembrane Elements. Cell Rep 2016;17(12):3319–32.
[39] Plaza-Menacho I, Morandi A, Robertson D, Pancholi S, Drury S, Dowsett M, et al. Targeting the receptor tyrosine kinase RET sensitizes breast cancer cells to tamoxifen treatment and reveals a role for RET in endocrine resistance. Oncogene 2010;29(33):4648–57.
[40] Roskoski R, Sadeghi-Nejad A. Role of RET protein-tyrosine kinase inhibitors in the treatment RET-driven thyroid and lung cancers. Pharmacol Res 2018;128:1–17.
[41] Subbiah V, Shen T, Terzyan SS, Liu X, Hu X, Patel KP, et al. Structural basis of acquired resistance to selpercatinib and pralsetinib mediated by non-gatekeeper RET mutations. Ann Oncol 2021;32(2):261–8.
[42] Plaza-Menacho I, Mologni L, Sala E, Gambacorti-Passerini C, Magee AI, Links TP, et al. Sorafenib functions to potently suppress RET tyrosine kinase activity by direct enzymatic inhibition and promoting RET lysosomal degradation independent of proteasomal targeting. J Biol Chem 2007;282(40):29230–40.
[43] Garner AP, Gozgit JM, Anjum R, Vodala S, Schrock A, Zhou T, et al. Ponatinib inhibits polyclonal drug-resistant KIT oncoproteins and shows therapeutic potential in heavily pretreated gastrointestinal stromal tumor (GIST) patients. Clin Cancer Res 2014;20(22):5745–55.
[44] Chen H, Ma J, Li W, Eliseenkova AV, Xu C, Neubert TA, et al. A molecular brake in the kinase hinge region regulates the activity of receptor tyrosine kinases. Mol Cell 2007;27(5):717–30.
[45] Shen T, Hu X, Liu X, Subbiah V, Mooers BHM, Wu J. The L730V/I RET roof mutations display different activities toward pralsetinib and selpercatinib. NPJ Precis Oncol 2021;5:48.
[46] Nakaoku T, Kohno T, Araki M, Niho S, Chauhan R, Knowles PP, et al. A secondary RET mutation in the activation loop conferring resistance to vandetanib. Nat Commun 2018;9(1). doi: https://doi.org/10.1038/s41467-018-02994-7.
[47] Subbiah V, Shen T, Tetzlaff M, Weissferdt A, Byers LA, Cascone T, et al. Patient-driven discovery and post-clinical validation of NTRK3 fusion as an acquired resistance mechanism to selpercatinib in RET fusion-positive lung cancer. Ann Oncol 2021;32(6):817–9.
[48] Ashkenazy H, Abadi S, Martz E, Chay O, Mayrose I, Pupko T, et al. ConSurf 2016: an improved methodology to estimate and visualize evolutionary conservation in macromolecules. Nucleic Acids Res 2016;44(W1):W344–50.